



Numerical analysis on the effect of surface roughness on the mechanical fields in polycrystalline aggregates

Yoann Guilhem, Stéphanie Basseville, François Curtit, Jean-Michel Stéphan,
Georges Cailletaud

► To cite this version:

Yoann Guilhem, Stéphanie Basseville, François Curtit, Jean-Michel Stéphan, Georges Cailletaud. Numerical analysis on the effect of surface roughness on the mechanical fields in polycrystalline aggregates. *Modelling and Simulation in Materials Science and Engineering*, 2018, 26 (4), 045004, 19 p. <10.1088/1361-651X/aab217>. <hal-01719022>

HAL Id: hal-01719022

<https://hal.science/hal-01719022v1>

Submitted on 28 Feb 2018

HAL is a multi-disciplinary open access archive for the deposit and dissemination of scientific research documents, whether they are published or not. The documents may come from teaching and research institutions in France or abroad, or from public or private research centers.

L'archive ouverte pluridisciplinaire **HAL**, est destinée au dépôt et à la diffusion de documents scientifiques de niveau recherche, publiés ou non, émanant des établissements d'enseignement et de recherche français ou étrangers, des laboratoires publics ou privés.



HAL Authorization

Numerical analysis of the effect of surface roughness on mechanical fields in polycrystalline aggregates

Yoann Guilhem¹, Stéphanie Basseville^{2,3}, François Curtit⁴,
Jean-Michel Stéphane⁴ and Georges Cailletaud³

E-mail: yoann.guilhem@ens-paris-saclay.fr

¹Laboratoire de Mécanique et Technologie (LMT), ENS

Paris-Saclay/CNRS/Université Paris-Saclay, 61 avenue du Président Wilson, 94235
Cachan, France

²Université de Versailles-Saint-Quentin-en-Yvelines, 45 avenue des Etats-Unis, 78035
Versailles cedex, France

³MINES ParisTech, PSL Research University, Centre des Matériaux, CNRS UMR
7633, BP 87, 91003 Evry Cedex, France

⁴EDF R&D, Département Matériaux et Mécanique des Composants, Avenue des
Renardières, 77818 Moret-sur-Loing Cedex, France

Abstract. This paper is dedicated to the study of the influence of surface roughness on local stress and strain fields in polycrystalline aggregates. Finite element computations are performed with a crystal plasticity model on a 316L stainless steel polycrystalline material element with different roughness states on its free surface. The subsequent analysis of the plastic strain localization patterns shows that surface roughness strongly affects the plastic strain localization induced by crystallography. Nevertheless, this effect mainly takes place at the surface and vanishes under the first layer of grains, which implies the existence of a critical perturbed depth. A statistical analysis based on the plastic strain distribution obtained for different roughness levels provides a simple rule to define the size of the affected zone depending on the rough surface parameters.

Keywords: Polycrystal, Crystal plasticity, Finite Element Analysis, Surface Roughness, Localization

Submitted to: *Modelling Simul. Mater. Sci. Eng.*

1. Introduction

Even though fatigue has been studied for several decades, it remains an open domain due to the wide variety of parameters that affect lifetime of structural components. Among these parameters, it has been observed at a macro scale that the surface state of a specimen comes into play in fatigue [1]. In the case of short fatigue cracks, which length is about a few grains, the microstructural features, such as grain boundaries and grain orientations, play a very important role in the early stages of crack growth. Under High Cycle Fatigue conditions, the incubation phase of these cracks (initiation and propagation through the first grains) may last more than half of the component total lifetime.

Experimental observations using Electron Back Scattering Diffraction (EBSD) technique [2, 3] and Atomic Force Microscope (AFM) [4, 5] give accurate information about the influence of local microstructure features on micro-crack nucleation. Nowadays, researchers are using nondestructive three-dimensional imaging techniques to investigate the role of local microstructure in the evolution of short fatigue cracks in Titanium polycrystals [6, 7]. Initiation is usually due to plastic strain localization along persistent slip bands at the surface, generated by crystallographic slip. The emergence of these bands at the surface leads to the formation of intrusions and extrusions [8], which can cause crack initiation by decohesion. The crystallographic orientation of the grains is the key parameter for these mechanisms, since it controls dislocation movements [9]. In polycrystals, the local stress and strain state differs from the macroscopic level due to heterogeneities linked with grain orientation and the associated stress redistribution resulting from local plastic flow. Finite Element Crystal Plasticity (FECP) is commonly used to determine local fields in order to study short fatigue crack initiation [10, 11, 12]. Previous works have shown the role of crystallographic orientation of the grains and neighborhood, as well as their position with respect to the surface on plastic strain localization [13, 14]. It is also shown that since intergranular redistribution is well captured, such simulations provide a rather good prediction of the location of the first fatigue crack, as well as critical slip systems at the origin of fatigue crack [15]. Dislocation Dynamics (DD) simulations give a finer description of local fields in the critical grain and around crack tip [9, 16], but without local stress deviation and redistribution due to neighboring grains, unless it is coupled with FECP.

The impact of the surface state resulting from industrial processes on fatigue life is governed by many parameters, among these, surface topology, residual stresses, surface hardening, recrystallization or phase transformation. Depending on materials, the type of surface finishing and the specific mechanical loadings, the effect of surface state can either be beneficial or detrimental [17]. Therefore, it becomes mandatory to characterize properly the loadings applied to the components on the one hand, and the effects of the industrial process on fatigue life on the other hand. After having introduced more and more physical aspects through a fine representation of the grains, the next step to go for a better modeling of surface fatigue damage is to account for the real local geometry. It is

worth noting that, even if the surface state is known to have an effect on initiation, only a little has been made in the literature to deliver a true quantitative comparison of various surface conditions. To name a few, Bayoumi et al. carried out fatigue experiments with samples polished with gradual quality. It turned out that fatigue initiation came earlier with as larger surface roughness [1]. The topological features such as the direction of grooves on a push–pull specimen can significantly decrease the fatigue limit up to 50%, specifically if the streaks are orthogonal to the loading axis [18]. LCF fatigue tests on 304L steel specimen with different surface states carried out under vacuum showed that increasing the Root Mean Square (RMS) of surface roughness by a factor of ten divided by two the time leading to fatigue crack initiation [19]. In addition, in the case of metastable materials, martensitic transformation can occur due to surface machining. The influence on local behavior is not negligible, and induces shorter service life under hydrogen atmosphere [20]. It has been proposed to model the effect of surface roughness by integrating a stress concentration factor within the fatigue crack initiation and propagation laws [21].

In fact, a true competition between the rough surface effect and the crystallographic effect takes place for damage development, that can be highlighted by means of numerical simulations. The improvement in experimental techniques now allows to capture real 3D microstructures, and to obtain strain field measurement, so that the real geometry can be introduced in FECP models, and the experiment–simulation comparison can be carried out on a local scale [22]. A previous study made on 304L steel, with real microstructure from EBSD mapping, considering surface roughness and local pre-hardening showed that these two parameters have respectively negative and positive effects on fatigue life [23]. Crystal plasticity finite element computations have also been used to investigate the evolution of surface roughness inside polycrystals under fatigue loadings [24]. Other numerical studies revealed that polycrystalline samples with cosine-like roughness profiles submitted to a cyclic loading exhibit a plastic strain localization in the roughness valleys, which emphasizes the role of initial surface state in micro-crack initiation [25]. However, according to their results, as the surface roughness increases for an initially flat aggregate, it tends to decrease if the surface is initially rough. In the contact and fretting context, the effect of roughness on friction can be crucial. For this purpose, the classical J_2 invariant theory is widely used [26, 27], but some studies based on FECP [28, 29] and DD [30] simulations are now also performed.

The purpose of the present study is to investigate the role of surface roughness, independently of all other parameters, on the fatigue crack incubation process (initiation and propagation within the first grain. This means that residual stresses created by the preliminary industrial process and their competition with microplasticity mechanisms will not be taken into account. The FECP calculations on polycrystalline aggregates will then be followed by a statistical analysis in order to characterize plastic strain localization at the surface and in the bulk of the material.

2. Numerical model

2.1. Constitutive equations

Méric–Cailletaud’s crystal plasticity model [31] available in the finite element suite Z-set [32] will be used, with a small strain framework, which seems reasonable, since, in our past experience, the amount of rotation of a slip plane is about 1° for 1% macroscopic strain. Each grain is considered as a single crystal and the displacement fields are supposed to be continuous at grain boundaries. Therefore stress discontinuities can appear at these sites. The strain rate tensor is partitioned into an elastic and a viscoplastic part:

$$\dot{\boldsymbol{\epsilon}} = \dot{\boldsymbol{\epsilon}}^e + \dot{\boldsymbol{\epsilon}}^p = \mathbf{C}^{-1} : \dot{\boldsymbol{\sigma}} + \dot{\boldsymbol{\epsilon}}^p \quad (1)$$

Cubic elasticity is defined by the fourth order tensor of elastic moduli \mathbf{C} , so that elasticity itself produces residual intergranular stresses.

The resolved shear stress τ^s is computed on each slip system s by means of the orientation tensor \mathbf{m}^s :

$$\tau^s = \boldsymbol{\sigma} : \mathbf{m}^s \quad (2)$$

$$\text{with } \mathbf{m}^s = \frac{1}{2} (\mathbf{l}^s \otimes \mathbf{n}^s + \mathbf{n}^s \otimes \mathbf{l}^s) \quad (3)$$

where \mathbf{n}^s is the normal to the slip plane and \mathbf{l}^s is the slip direction.

The viscoplastic strain rate tensor is defined as the sum of the contributions of all the slip systems s . Each viscoplastic slip rate $\dot{\gamma}^s$ is given by a power law, function of the resolved shear stress, the critical resolved shear stress τ_0 and two variables, x^s for kinematic hardening and r^s for isotropic hardening.

$$\dot{\boldsymbol{\epsilon}}^p = \sum_s \dot{\gamma}^s \mathbf{m}^s \quad (4)$$

$$\dot{\gamma}^s = \text{sign}(\tau^s - x^s) \dot{v}^s \quad (5)$$

$$\dot{v}^s = \left\langle \frac{|\tau^s - x^s| - r^s - \tau_0}{K} \right\rangle^n \quad (6)$$

$$\text{with } \langle \bullet \rangle = \begin{cases} \bullet & \text{if } \bullet > 0 \\ 0 & \text{if } \bullet \leq 0 \end{cases}$$

where K and n are the parameters for viscosity, \dot{v}^s stands for slip rate, v^s is the cumulated viscoplastic slip on slip system s .

Hardening depends on two internal state variables, α^s for kinematic and ρ^s for isotropic hardening, as described by equations 7 to 10. This framework offers a single set of active slip systems, and avoids complex procedures attached to the definition of

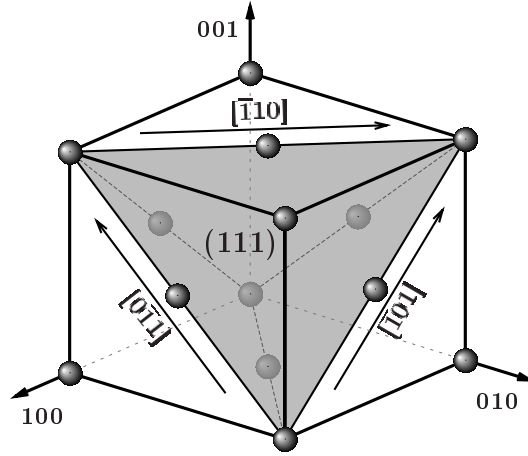


Figure 1: Octahedral slip systems in FCC crystal.

slip activity for the time independent plastic case [33].

$$x^s = c\alpha^s \quad (7)$$

$$r^s = bQ \sum_r h_{sr} \rho^r \quad (8)$$

$$\dot{\alpha}^s = \left(\text{sign}(\tau^s - x^s) - d\alpha^s \right) \dot{v}^s \quad (9)$$

$$\dot{\rho}^s = (1 - b\rho^s) \dot{v}^s \quad (10)$$

where c and d are material parameters for kinematic hardening, Q and b are material parameters for isotropic hardening. Self-hardening and latent hardening between different slip systems are characterized by the components of the interaction matrix, noted h_{sr} . The material of the study is an austenitic stainless steel, the crystallographic structure of which is FCC, and where slip operates on octahedral slip systems, defined by the family of four $\{111\}$ slip planes, and by the slip directions $\langle 110 \rangle$, resulting in twelve slip systems (figure 1). The corresponding interaction matrix is defined by six material parameters h_i [34]. All the material parameters have already been identified for a 316L Stainless Steel in a previous study [14].

2.2. Meshes of aggregates with flat and rough free surfaces

The polycrystalline aggregate reference mesh used here (figure 2) is built by Voronoi tessellation as explained in a previous study [14]. The aggregate is composed of 291 grains, its size is $250 \mu\text{m} \times 250 \mu\text{m} \times 125 \mu\text{m}$. The mesh consists of 626 899 nodes and 454 673 elements.

A rough surface is generated from a one-dimensional roughness profile measured on a brushed surface state component, which mainly consists of parallel streaks (see figures 3a, 3b and 3c). The roughness parameters characterizing the profile of the measured brushed surface are given in table 1.

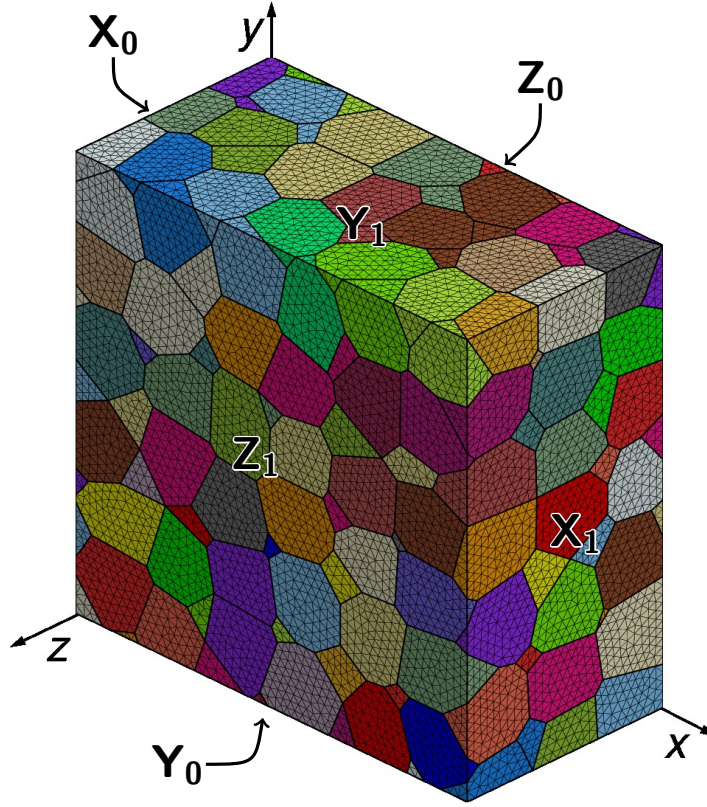


Figure 2: Mesh of the 291 grain aggregate with the definition of each face.

A representative section of the roughness profile is selected (noted $f(l)$ in figure 3c) and is then extended along x axis to produce a surface $g(x, y)$, as shown by figure 3d. A Brownian noise is finally added to provide the final synthetic rough surface $h(x, y)$ (figure 3e). The mesh is generated from the reference flat surface mesh, by translating the nodes along z axis, which is normal to the reference flat surface. Surface nodes are moved, as well as bulk nodes, in order to avoid the appearance of degenerated elements, since the element size (about $5 \mu\text{m}$) is smaller than the defects due to roughness (about $12 \mu\text{m}$). From the free surface Z_1 (where the node displacement is equal to the interpolated rough surface height), the node displacement is linearly linked to the distance to the free surface d_{surf} , until a maximal depth $d_{\text{max}} = 62.5 \mu\text{m}$ below the free surface (where the displacement becomes nil), according to:

$$\Delta z(x, y, d_{\text{surf}}) = k_r \cdot \frac{d_{\text{max}} - d_{\text{surf}}}{d_{\text{max}}} \cdot h(x, y) \quad (11)$$

where k_r is the scalar defining roughness magnitude. $k_r = 0$ corresponds to the flat surface, meanwhile $k_r = 1$ will create the brushed surface with the full roughness.

2.3. Boundary conditions and loading cases

A two cycle tension-compression load is considered with a load ratio $R_\sigma = -1$. Three kinds of cyclic loading are investigated ; uniaxial in x direction, uniaxial in y direction

Table 1: Roughness parameters of the brushed surface state.

Roughness parameter	Value [μm]
Maximum roughness height R_t	14.30
Arithmetic mean value R_a	1.88
Root mean-square-average R_q	2.38

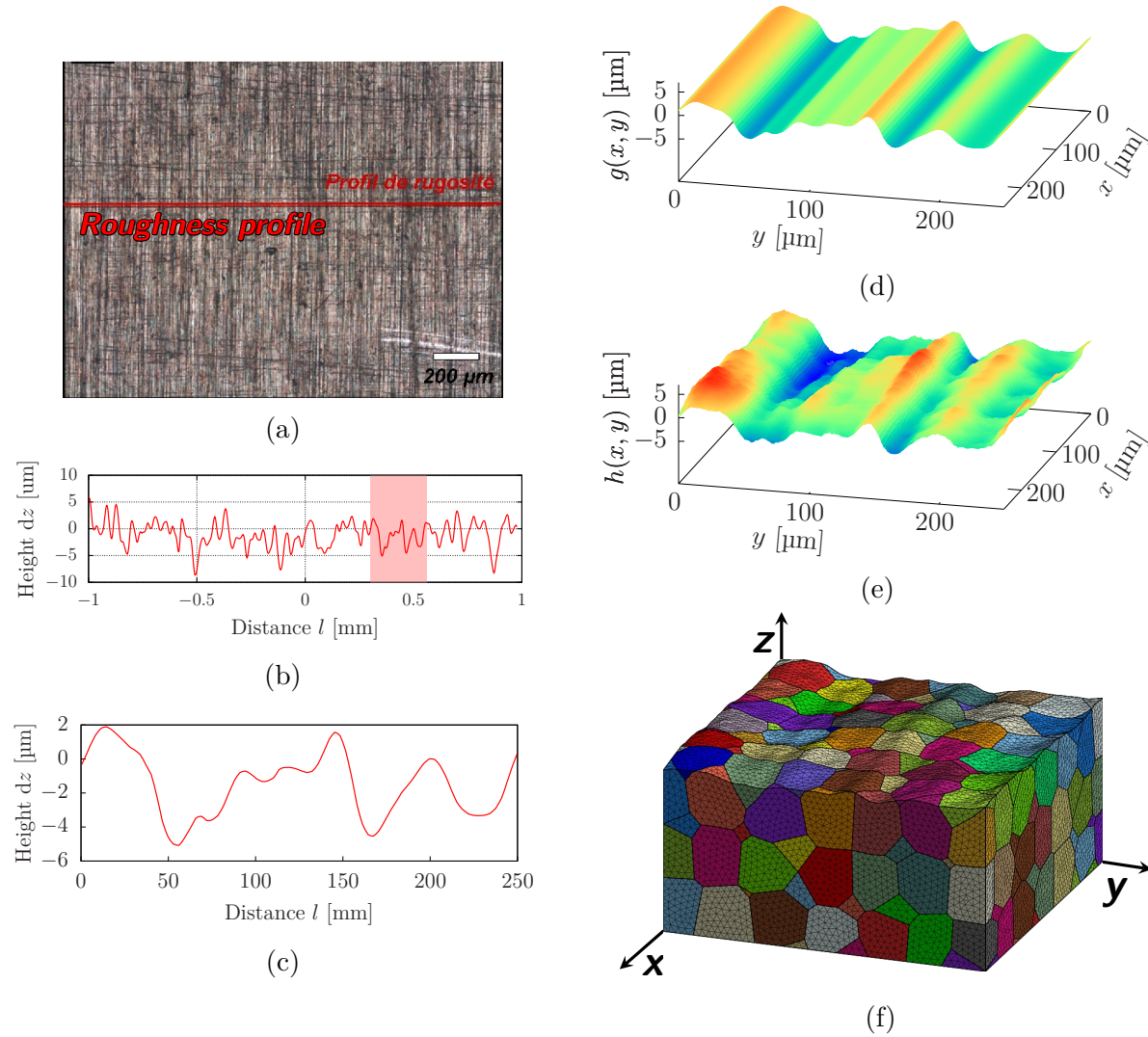


Figure 3: Surface state studied in this paper. (a) Optical microscope image of the brushed surface with a red line along the (b) one-dimensional roughness profile, all provided by Le Pécheur et al. [23, 35]. (c) Selected part of the roughness profile for the synthetic surface generation. (d) Initial surface extended from profile and (e) final surface provided after Brownian noise addition. (f) Resulting rough mesh.

and biaxial with the same equivalent strain as uniaxial. For each case, symmetric boundary conditions are applied on hidden faces X_0 , Y_0 and Z_0 (figure 2), and face Z_1 is a free surface. The Boundary Conditions (BC) on faces X_1 and Y_1 are set depending on the considered loading case :

a) Uniaxial-x

- Face X_1 : $\pm 0.5 \mu\text{m}$ cyclic displacement to obtain a macroscopic deformation $E_{xx} = \pm 0.2\%$
- Face Y_1 : uniform normal displacement

b) Uniaxial-y

- Face X_1 : uniform normal displacement
- Face Y_1 : $\pm 0.5 \mu\text{m}$ cyclic displacement to obtain a macroscopic deformation $E_{yy} = \pm 0.2\%$

c) Biaxial-eq

- Face X_1 : $\pm 0.35 \mu\text{m}$ cyclic displacement to obtain a macroscopic deformation $E_{xx} = \pm 0.14\%$
- Face Y_1 : $\pm 0.35 \mu\text{m}$ cyclic displacement to obtain a macroscopic deformation $E_{yy} = \pm 0.14\%$

In uniaxial cases (a) and (b), a multipoint constraint is applied to preserve a zero resulting force for the faces with an uniform normal displacement, so that all faces X_0 , X_1 , Y_0 and Y_1 remain planar.

3. Results and discussion

The following local variables are investigated:

- $\gamma_{cum} = \sum_s v^s$: the sum of the accumulated plastic slip on all slip systems
- σ_{mises} : the von Mises equivalent stress
- N_γ : the number of active slip systems, defined by

$$\dot{v}^s > \dot{\gamma}_c = 0.75 \frac{M_T \cdot \dot{\epsilon}_{macro}}{5} = 1.86 \times 10^{-3} \text{ s}^{-1} \quad (12)$$

where $\dot{\gamma}_c$ is a critical threshold corresponding to 75 % of the average plastic strain rate. It depends on the Taylor factor M_T (about 3.1 for FCC polycrystals), the macroscopic strain rate $\dot{\epsilon}_{macro}$, the number of independent internal variables needed to accommodate plastic strain (5 in our case).

To compare the results obtained on rough meshes to the reference flat case, we provide three indicators, defined for a generic local variable X :

- the ratio between the local value obtained in the rough case and the result of the reference calculation (flat aggregate), also called “perturbation ratio”, defined at each integration point by:

$$R(X, k_r) = \frac{X(k_r)}{X(k_r = 0)} \quad (13)$$

Table 2: IRPI for various maximal depths d_{\max} (BC grains are not taken into account).

k_r	d_{\max} [μm]	γ_{cum}	σ_{mises}
1.0	31.25	1.052×10^{-1}	2.832×10^{-2}
1.0	62.50	1.055×10^{-1}	2.959×10^{-2}
1.0	125.00	1.103×10^{-1}	3.213×10^{-2}

- the difference between the local value obtained in the rough case and the result of the reference calculation (flat aggregate), defined at each integration point by:

$$D(X, k_r) = X(k_r) - X(k_r = 0) \quad (14)$$

- the Induced Roughness-Perturbation Indicator (IRPI), which characterizes the influence of the roughness on the local mechanical fields. It is globally defined for a zone of interest (e.g. whole mesh, surface grains, a specific grain, etc) of each rough mesh by:

$$\text{IRPI}(X, k_r) = \frac{1}{N_{\text{IP}}} \sum_{i=1}^{N_{\text{IP}}} \left| \frac{X(k_r) - X(k_r = 0)}{X(k_r = 0)} \right| \quad (15)$$

where N_{IP} is the total number of integration points of the zone of interest.

In the following, each time statistical data will be given, only the integration points from the grains which are not in contact with boundary conditions will be considered. It has been already shown that these grains are not suitable for statistical analysis due to the constraint on local displacement applied at the boundaries [14].

3.1. Roughness effect for streaks perpendicular to the loading direction

A selection of the results obtained under one-dimensional loading in y direction is shown in figure 4, where the contour maps at the free surface Z_1 are shown and thus can be compared to the roughness contour maps with various roughness levels. The reference results, provided by the computation on the initial flat mesh are also shown in figures 4b to 4d.

The value of d_{\max} , the depth of the zone where node are displaced, initially depends on the maximal roughness range, which is about $12 \mu\text{m}$. The element size being about $5 \mu\text{m}$, it is mandatory to spread the node displacement on a layer of 10 elements to avoid badly-shaped or degenerated elements. Table 2 presents IRPI values for accumulated slip and von Mises stress, using various d_{\max} values. It has a very small influence on the global perturbation of the local fields. Using a $62.5 \mu\text{m}$ maximal depth, equal to half the total aggregate thickness, no badly-shaped elements are created. We will then always use this value in the following.

Table 3 sums up the IRPI of the studied variables for the various roughness intensities considered in this paper. According to this indicator, plastic strain and equivalent stress linearly depend on roughness intensity (see figure 5).

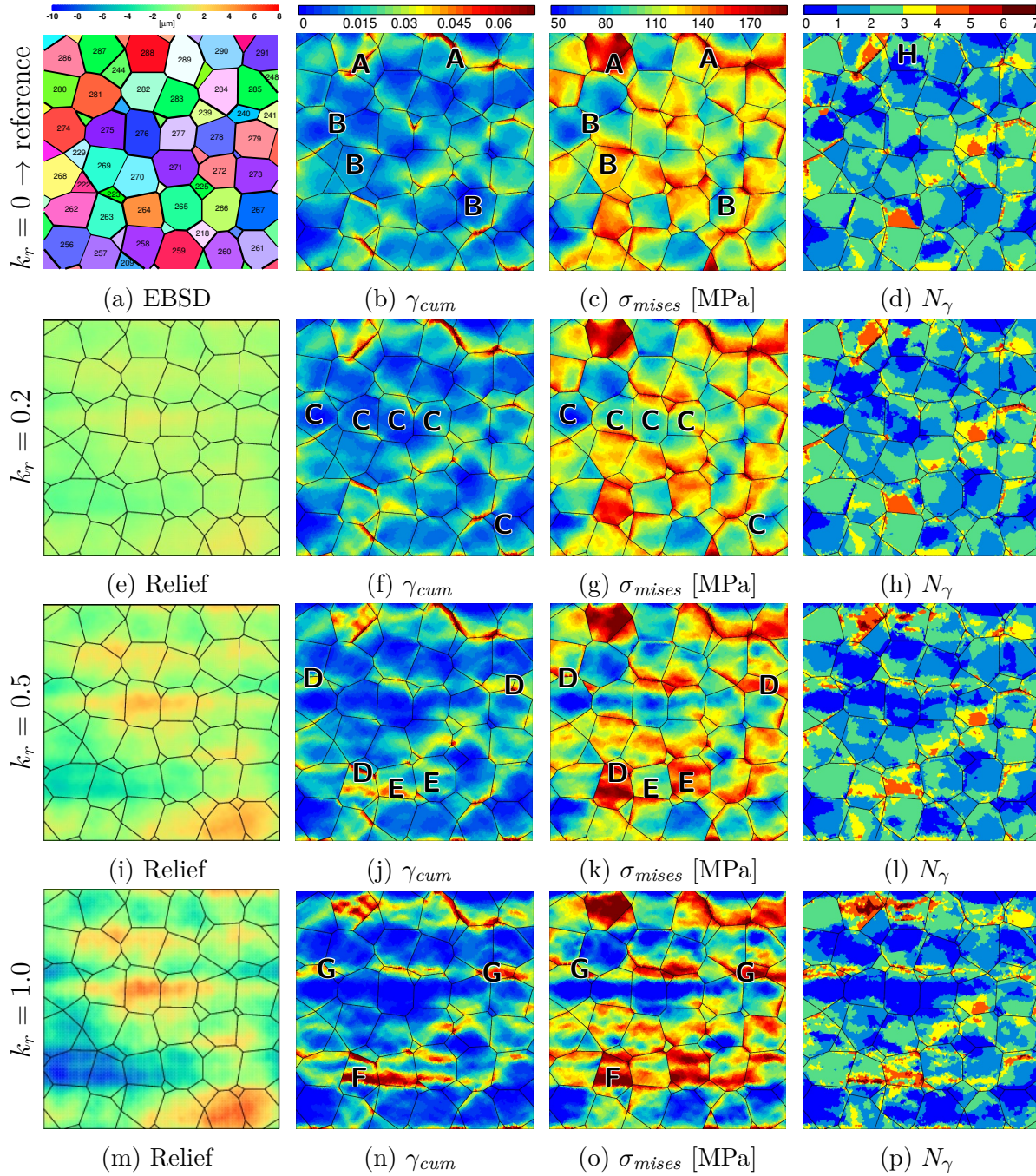
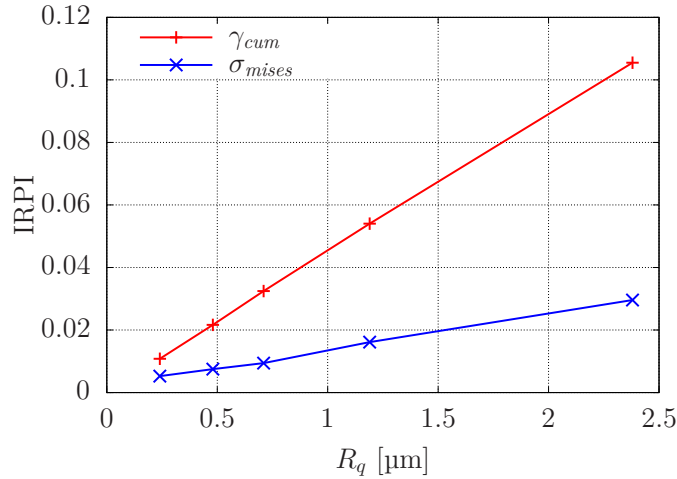


Figure 4: Influence of the surface roughness on the local mechanical fields when the loading direction is orthogonal to the streaks (uniaxial-y loading case \uparrow). (a) EBSD map of the free surface. (b, c, d) Local fields of the flat case [14]. (e, i, m) Roughness maps for each rough case. (f-h, j-l and n-p) Local fields of plastic strain γ_{cum} , equivalent stress σ_{mises} and number of active slip system N_γ for respectively cases $k_r = \{0.2; 0.5; 1.0\}$.

Table 3: IRPI for various roughness intensities (BC grains are not taken into account).

k_r	R_q [μm]	γ_{cum}	σ_{mises}
1.0	2.38	1.055×10^{-1}	2.959×10^{-2}
0.5	1.19	5.402×10^{-2}	1.614×10^{-2}
0.3	0.71	3.248×10^{-2}	9.412×10^{-3}
0.2	0.48	2.164×10^{-2}	7.492×10^{-3}
0.1	0.24	1.080×10^{-2}	5.277×10^{-3}

Figure 5: Evolution of IRPI depending on R_q , describing roughness intensity.

The sum of accumulated plastic slip over all slip systems γ_{cum} , characterizes the intensity of plastic flow (figures 4b, 4f, 4j and 4n). First, we compare flat (figure 4b) and $k_r = 1$ cases (figure 4n). The localization band patterns, oriented at 45° with respect to the loading direction, classically observed on flat aggregates are modified in presence of roughness. For a flat surface case, the critical areas are determined by the grains favourably oriented for slip activity, by grain boundaries and triple points, whereas for rough surfaces, these zones are replaced by the valleys introduced by roughness. The plastic strain localization essentially occurs at notch roots. It is then linked to local geometry more than local crystallographic texture. Nevertheless, discontinuities still appear at some grain boundaries, even at the bottom of the valleys, and the most critical points do not always correspond to the lowest zones of the surface. It demonstrates that crystal plasticity is still driving some aspects of localization and that a competition between crystallography and “notch” effect is taking place. For intermediate values of the roughness intensity, from $k_r = 0.2$ to $k_r = 1$ (figures 4f, 4j and 4n), a progressive transition between the two types of localization is exhibited. The main observations are the following:

a) In figures 4b, 4f, 4j and 4n, the crystallographic character remains predominant in

areas with only little geometrical changes. In this case, well marked slip zones at grain boundaries remain active (points A), and the grains with a low plasticity level keep the same type of cumulated slip (points B). In some other places, the flat surface becomes a hill, so that the plastic flow gets smaller and smaller when roughness is more and more marked (points C), reaching all blue lines of grains for the maximum roughness intensity. The presence of streaks is able to create new plastic zones at grain boundaries or to reinforce preexisting plasticity (points D). New plastic zones can also be seen inside grains (points E). In some cases, the development of plasticity is clearly linked to the deformation of a neighboring grain (point F). It can be checked that the local behavior is not determined by the absolute position of the node on the brushed surface with respect to the initial flat surface, but the position with respect to the immediate surrounding: plasticity develops along line G-G, along a not so well marked streak; due to the W-shape of the streak in grains E and F, plastic slip remains low in the middle of the W-shape, even if the translation with respect to the initial surface is important. To summarize the effect of streak introduction, it can be stated that the maps of cumulated slip exhibit the highest plasticity levels at grain boundaries and, that, even at a low strain level, slip bands can be observed, making a 45° angle with the tensile direction. This morphology tends to be replaced by horizontal slip bands at the notch of the streaks.

- b) Figures 4c, 4g, 4k and 4o show the corresponding changes in von Mises stress maps. For A and B zones, where plastic flow was not affected by the roughness, the von Mises stress is not affected as well. For the case of hills, like the line of grains C-C, the von Mises stress becomes lower and lower when roughness increases. The strain localization observed at points D tends to increase the stress gradient accordingly. The stress gradients are also higher due to plastic zone development (E, F, G type). To summarize the effect of streaks, (i) for a flat surface, the level of the von Mises stress is almost determined grain by grain, due to crystallographic orientation, (ii) meanwhile the stress contours are given by the topology, with higher gradients, marked low-level on hills and high-level at notches.
- c) The comparison of figures 4d, 4h, 4l and 4p shows that the number of active slip systems is less uniform for a rough surface than for a flat one. Large grains with multiple slip (grain H) are affected by the geometrical changes, so that plasticity becomes more localized. To sum up, the presence of hills tends to “clean” the slips that are already weak for the flat surface, and the notch roots generate stress concentrations that promote the activation of new systems, with a large Schmid factor, so that they are predominant for the higher roughness levels.

3.2. Streaks parallel to loading direction and biaxial loading

Computations are performed on the flat mesh and rough mesh (with brushed surface state, $k_r = 1$) of the previous section, with the same grain shape, grain orientations set and geometry of the rough surface, but with different loading conditions as explained

in section 2.3.

3.2.1. Uniaxial-x loading Figure 6 shows the local mechanical fields for the flat and rough surfaces, for the uniaxial-x loading case. The loading direction is now collinear to the streak direction. Due to the different loading cases, the critical zones are not the same as in figure 4, even for the flat surface, and, since the perturbation coming from the geometry is weaker, most of the localization patterns remain the same in reference and rough cases. The following behaviors are then observed:

- a) For both flat and rough surfaces, a series of grain boundaries (denoted A) present intense slip activity (figures 6b and 6f), meanwhile most of the grains (see for instance B) have a low plasticity level. The effect of hills is less sensitive than for figure 4, except for grain C. The cases corresponding to a newly active grain boundary or to a reinforced plastic flow inside a grain are very rare (respectively points D and E). The most active plastic zone in F is mainly due to a cross effect with boundary conditions. To sum up, the effect of roughness is low for this loading case. Interestingly, even a plastic localization band at 45° from the loading direction is still preserved on the rough surface case (see line G-G). The main difference between flat and rough surfaces is the fact that the field is less smooth for the rough surface than for the flat.
- b) The perturbation coming from the introduction of roughness is more sensitive on von Mises stress contour maps (figures 6c and 6g). For instance, zones with a rather uniform value, like the four grains H, present stress gradients when the surface is no longer flat. In grains, such as I, that present uniform gradient for the flat surface, several maxima and/or minima can appear for the rough surface case. The most important effect is observed for grains such as J, located at the end of the streak, so that the geometric perturbation plays the role of a notch perpendicular to the loading direction.
- c) The comparison of the active slip system maps is made in figures 6d and 6h. As for the previous fields, the difference between the two is mainly a larger scatter in presence of roughness. Unlike loading perpendicular to the streak, the presence of a larger scatter for the rough surface does not come with a visible decrease of the number of active slip systems.

3.2.2. Biaxial-eq loading Figure 7 shows the local mechanical fields for the flat and rough cases under biaxial-eq loading case. Unlike uniaxial loading, there is no 45° localization bands in the reference solution, since all the in-plane directions are equivalent at a macroscale. This is also the reason why no preferential orientation can be found for critical grain boundaries on the flat surface case. The localization patterns produced by the geometrical changes will then be much more sensitive than in the previous cases.

The main remarks are as follows:

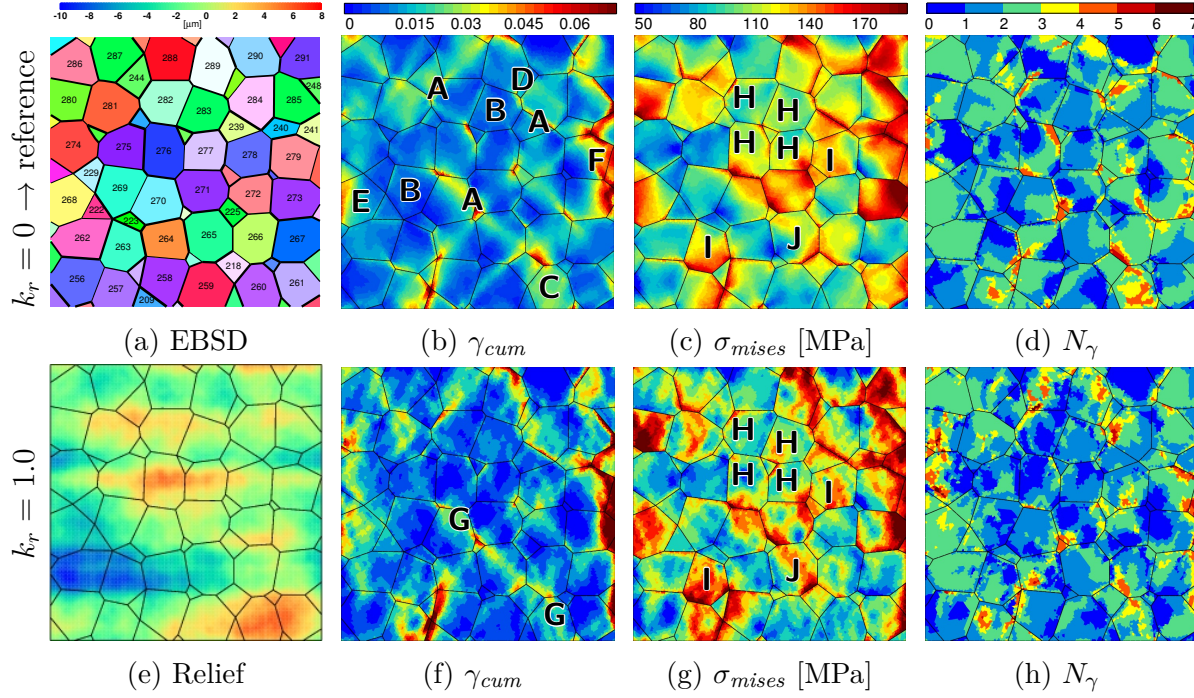


Figure 6: Influence of a rough surface on the local mechanical fields when the loading direction is collinear to the streaks (uniaxial-x loading case \Leftrightarrow).

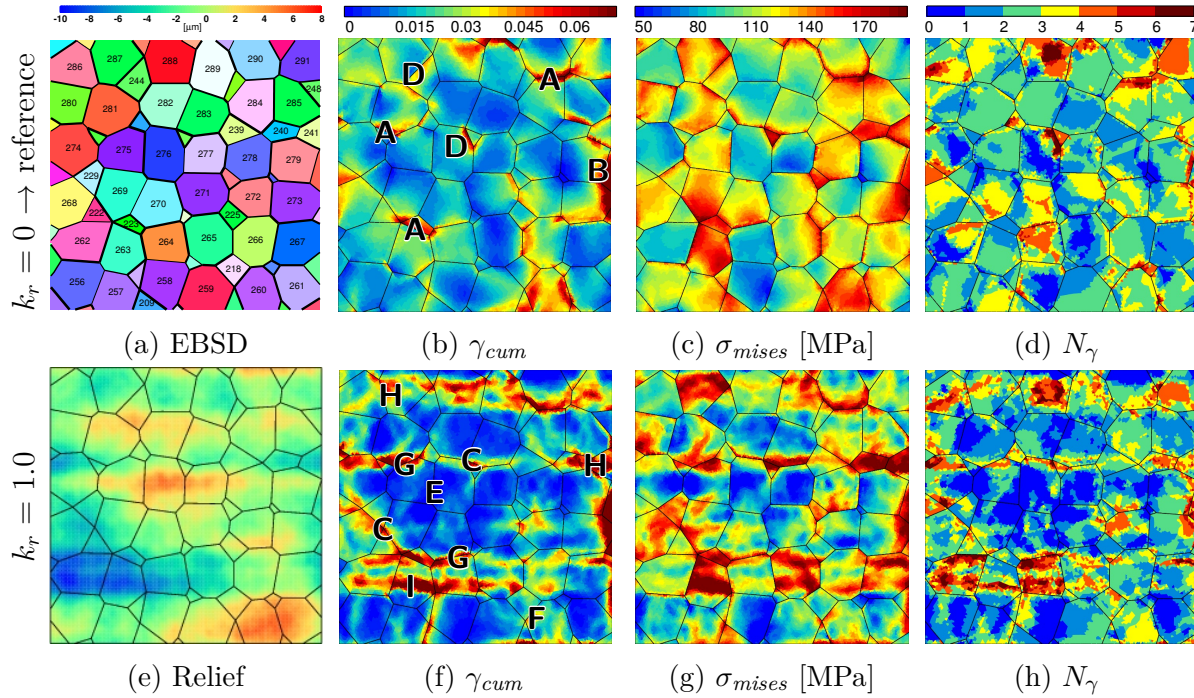


Figure 7: Influence of a rough surface on the local mechanical fields when the loading is equally combined of orthogonal and collinear directions to the streaks (biaxial-eq loading case).

Table 4: IRPI for the different loading cases, each with $k_r = 1$ (BC grains are not taken into account).

Load	γ_{cum}	σ_{mises}
uniaxial-y	1.069×10^{-1}	2.951×10^{-2}
uniaxial-x	7.228×10^{-2}	1.953×10^{-2}
biaxial-eq	1.047×10^{-1}	3.033×10^{-2}

- a) Some of the grain boundaries that present slip activity on the reference calculation remain active with the rough surface (figures 7b and 7f), for areas affected by the boundary conditions (B), but also for “current” conditions (points A). Nevertheless newly active grain boundaries appear due to the rough surface effect (C), meanwhile some of them disappear (D). The main effect on grains themselves is that, due to hills, slip is suppressed in zones with a low initial plastic activity (E), or highly reduced in the active zones (F). The general result is that the zones that have marked slip activity amazingly follow the topology of the rough surface, with slip along all the main streaks. They may coincide with grain boundaries (like G), but most of them go through the grains (H), underlining the already mentioned W-shape for the grain (I).
- b) The von Mises stress maps produced under biaxial load (figures 7c and 7g) for the flat aggregate do not present any disturbed area along its right edge, as it does for uniaxial-x case. The result is close to the uniaxial-y case, where most of the grains present a uniform stress level or a low gradient. The field obtained with the rough surface exhibits the strongest gradients among the three loading cases. In fact, the stress map matches with the plastic slip contours. It can be explained by the fact that the stress concentration due to topology, already present in the uniaxial-y case, is magnified by the two-dimensional character of the loading. It was already shown in a former study that a biaxial loading generates more plastic strain and thus is more damaging than a reference uniaxial loading at the equivalent strain range [14].
- c) The map of the number of active slip systems (figures 7d and 7h) shows that slip heterogeneity is enhanced by roughness, since biaxial loading allows more slip systems to have a large Schmid factor.

3.3. Roughness influence inside the material

Fatigue crack growth is a 3D problem, and the growth rate obviously depends on the stress and plastic strain fields in the bulk of the material. The roughness effect must then be investigated not only at the surface, but also in depth. Figure 8 shows plastic strain maps for several xz cutting planes (three different values of x) for the flat and $k_r = 1.0$ cases under uniaxial-y loading. The local difference $D(\gamma_{cum}, 1.0)$ map is also plotted to highlight the perturbation zones. For the sake of brevity, only plastic strain

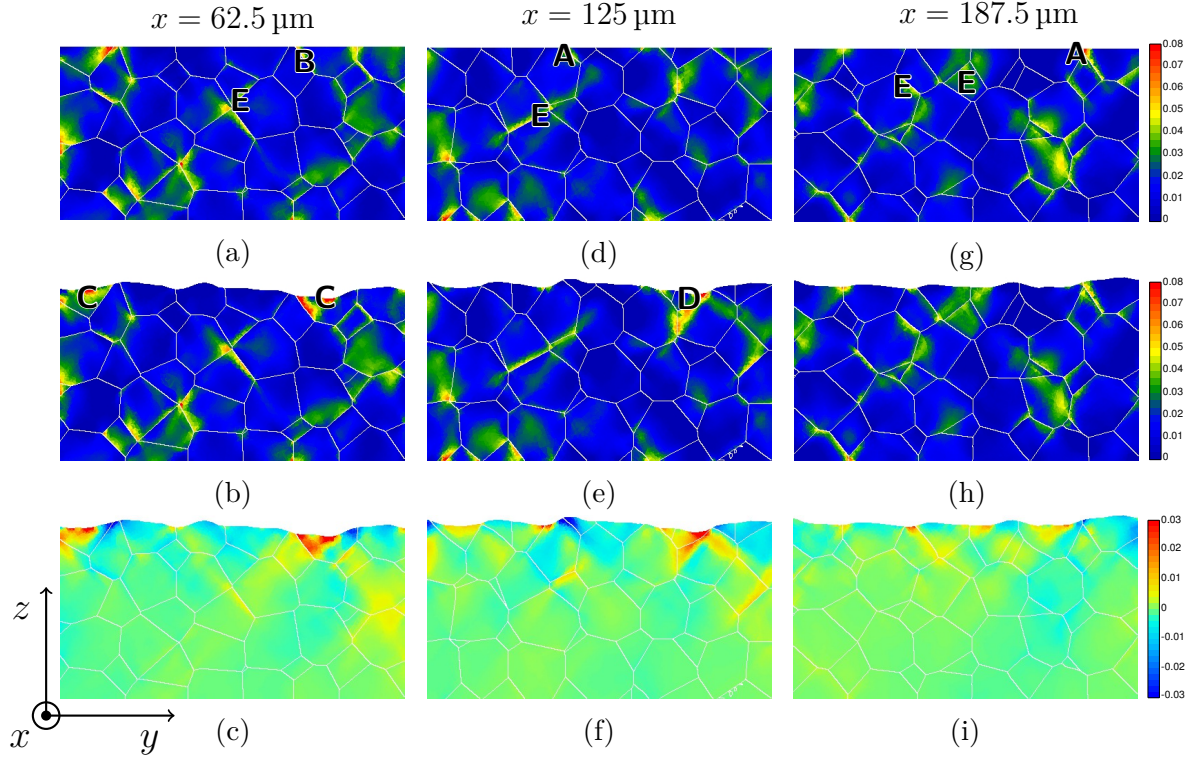


Figure 8: Clipped views of the plastic strain fields under uniaxial-y loading case in 3 planes $x = 62.5 \mu\text{m}$, $125 \mu\text{m}$ and $187.5 \mu\text{m}$, corresponding to each column. (a), (d) and (g) Flat mesh (reference). (b), (e) and (h) Brushed mesh. (c), (f) and (i) Difference between the local plastic strain fields for the flat and the brushed mesh.

is plotted, but the conclusions would be the same when considering stress fields. This allows to qualitatively examine how the localization patterns are modified depending on the distance to the free surface. Like for the surface observations, the present contours show:

- a) grains boundaries where plastic flow is smaller for the rough surface (A),
- b) grain boundaries where pre-existing plasticity is reinforced by roughness (B),
- c) some zones inside the grains where roughness generates plastic flow (C) which did not occur with a flat surface,
- d) complex arrangements mixing grain boundary effect, surface effect and topology (D).

When inspecting zones beyond the first layer of grains below the surface, the differences between flat and rough cases vanish. The effect of surface roughness is then amazingly limited to a certain depth, comparable to grain size. Typical patterns like (E) remain unchanged on the rough surface maps. Since the two meshes have the same connectivity (the “rough” case is obtained by a deformation of the flat mesh, preserving mesh topology), one can easily calculate the difference $D(\gamma_{cum})$ between both cases at each integration point. The corresponding maps (figures 8c, 8f and 8i) exhibit almost null values for the second grain layer and beyond.

3.4. Statistical analysis

The observations made in the previous section demonstrate the existence of a limited zone, in terms of depth, which is affected by the presence of surface roughness. To quantify the depth of this affected zone, a statistical analysis is proposed. It is based on the plastic strain distribution inside the aggregate for a wider range of roughness intensities, namely $k_r = \{0.1, 0.2, 0.3, 0.5, 1.0\}$, each one submitted to uniaxial-y loading case. For each integration point in the material element, the modification of local plastic strain due to roughness is characterized by the “perturbation ratio” $R(\gamma_{cum}, k_r)$ between the value obtained in the rough case, and the value resulting from the reference calculation (flat aggregate).

Multiple integration points zones were delimited using the distance to the free surface d_{surf} (which is always defined in the flat aggregate configuration), each zone corresponding to a $5\text{ }\mu\text{m}$ interval, where the distribution of the local perturbation ratio has been studied. Only a few are presented here: zone 1 ($d_{surf} \leq 5\text{ }\mu\text{m}$), zone 3 ($10\text{ }\mu\text{m} \leq d_{surf} \leq 15\text{ }\mu\text{m}$) and zone 5 ($20\text{ }\mu\text{m} \leq d_{surf} \leq 25\text{ }\mu\text{m}$). Normal distribution functions (defined by mean and standard deviation of the values in the investigated zone) and Generalized Extreme-Value (GEV) distribution functions [36] are compared with the computed distributions (figure 9). Most of the data distributions are in good agreement with the normal distribution function, so that it can be considered that the perturbation follows a Gaussian distribution centered on 1 for each zone. In zones 3 and 5 (figures 9b, 9e and 9h). This is not the case for zone 1, which is the most affected by roughness, where the fields are hardly fitted by normal distributions, but are better represented by GEV functions. These functions are able to reproduce Fréchet, Gumbel or Weibull distribution using a shape factor ξ :

$$G(x) = \begin{cases} \exp\left(-(1 + \xi x)^{-1/\xi}\right) & \text{if } \xi \neq 0, \forall x / 1 + \xi x > 0, \\ \exp(-\exp(-x)) & \text{if } \xi = 0. \end{cases} \quad (16)$$

This function has already been used to fit the distribution of a fatigue parameter for a large range of 2D polycrystal realizations [37]. Having in hands these observations, such a statistical representation might be a good candidate to investigate the effect of roughness from a statistical point of view on a large set of polycrystalline aggregate realizations with various roughness states. It is worth mentioning that the fitted values of the shape factor ξ in figure 9 are always negative, which corresponds to a Weibull scheme. Near the surface, in zone 1, ξ is getting closer to zero, as it is for a Gumbel distribution. This observation agrees with the statistical analysis performed by Hor et al., using the criteria of Matake and Dang Van as critical fatigue parameters [37].

The perturbation ratio $R(\gamma_{cum}, k_r)$ is plotted for each integration point as a function of the distance to the free surface in figure 10a, for various k_r values. According to the previous observations, the scatter is higher for increasing roughness values. The variations of $R(\gamma_{cum}, k_r)$ produced with $k_r = \{0.1, 0.2\}$ remain in a factor 2. For $k_r = 0.3$, values like 3 and 0.1 are reached. For $k_r = \{0.5, 1\}$, some points near the

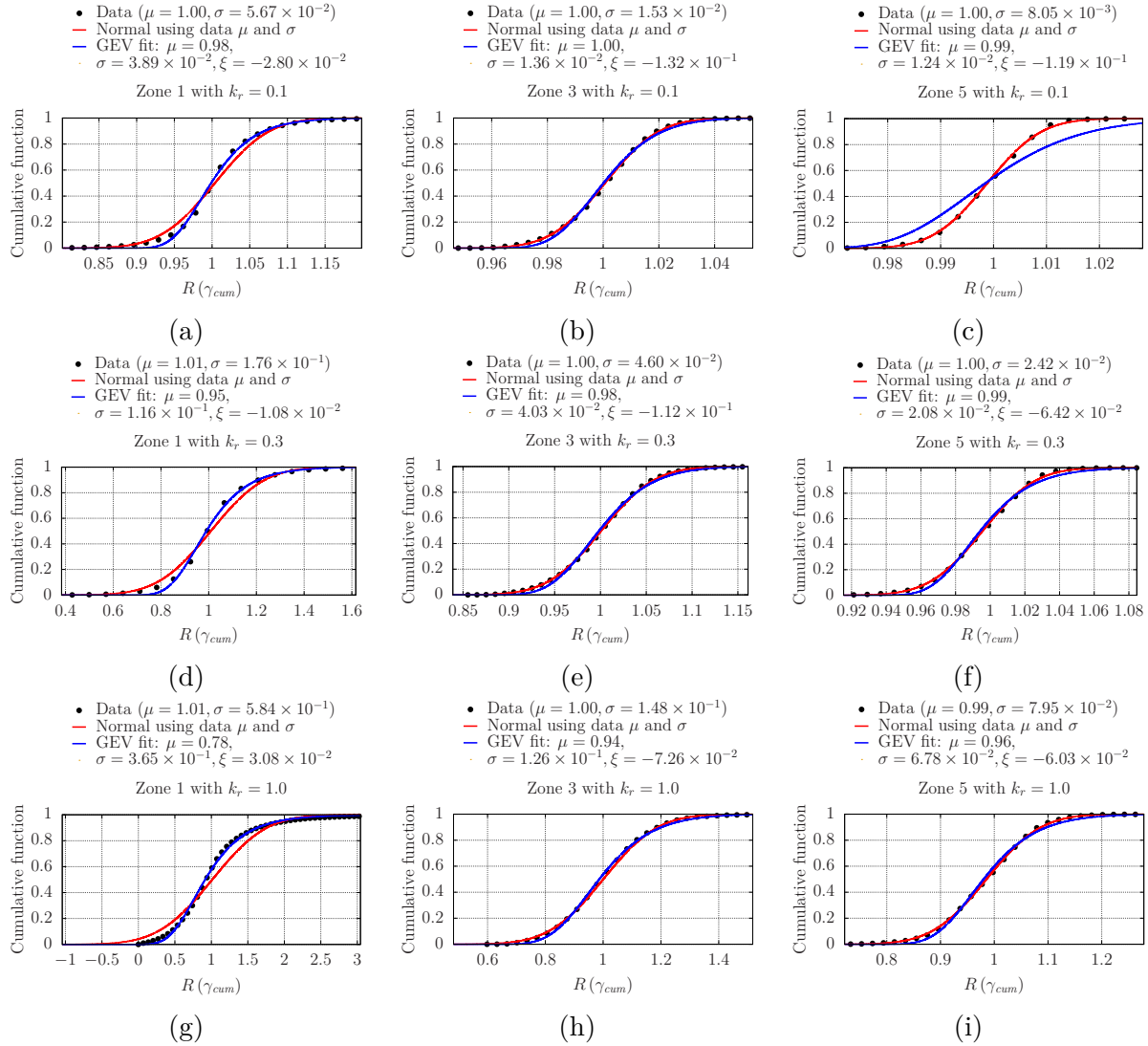


Figure 9: Fit for ratio $R(\gamma_{cum})$ cumulative distributions over three depth intervals for different roughness intensities k_r .

surface ($0 \mu\text{m} < d_{\text{surf}} < 4 \mu\text{m}$ for $k_r = 1$) are elastic for the rough surface case meanwhile they are plastic for the flat surface, so that $R(\gamma_{cum}, k_r) = 0$. The highest value obtained for $R(\gamma_{cum}, k_r)$ is 11.282 and 6 values are greater than 10. In any case, all the curves converge toward 1 in the bulk, showing that the fields are no longer disturbed for a relatively short distance.

Figure 10b shows the evolution of the standard deviation depending on the distance to the free surface d_{surf} . The critical value d_{crit} defines the distance to the free surface for which the standard deviation of the perturbation ratio $R(\gamma_{cum})$ is less than 0.1. This condition implies that approximately 99.7% of the values at this depth are affected by a ratio lower than 5×10^{-3} in the case of a Gaussian distribution.

Such a quantitative approach allows to show the correlation between the RMS of the rough surface, denoted by R_q , and the critical distance determined in figure 10c.

Amazingly, the evolution is linear with a small offset. It shows that surface roughness has no significant effect when the RMS of a brushed surface is less than $0.25\text{ }\mu\text{m}$ in the present conditions (e.g. material behavior, grain size). For a RMS of $2.5\text{ }\mu\text{m}$, the critical distance is comparable to one half of the grain size ($50\text{ }\mu\text{m}$).

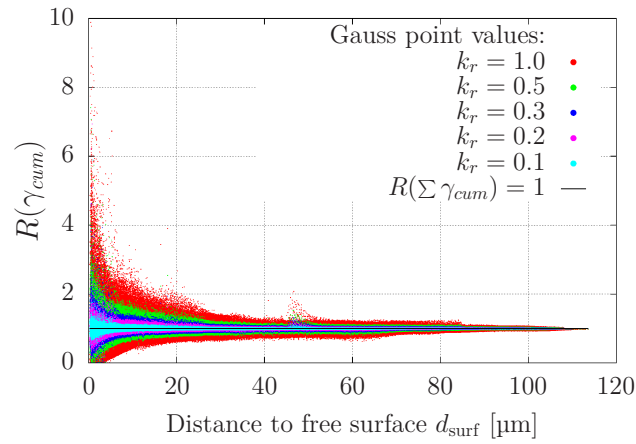
4. Conclusion

In this paper, we used Finite Element Crystal Plasticity to characterize the effect of surface roughness on the local mechanical fields at the surface of polycrystalline aggregates. A drastic change in the localization patterns was observed when comparing the results on flat and brushed surfaces, where plastic strain tends to localize at the bottom of the relief valleys. The competition between the local crystalline orientation and the geometry of the surface roughness was investigated. The strong influence of surface streaks has been evaluated for several types of one-dimensional and two-dimensional loading paths. It has been found in agreement with former literature results [18]. A volumetric analysis showed that this effect seems to be restricted to the first layer of grains below the surface. To give a quantitative relation between the roughness and the critical zone influenced by a brushed surface, many computations with gradual RMS were carried out, followed by a statistical analysis. The results showed that the thickness of this affected layer below the surface is linearly correlated to the surface RMS by a factor close to 16 in the conditions of our calculations.

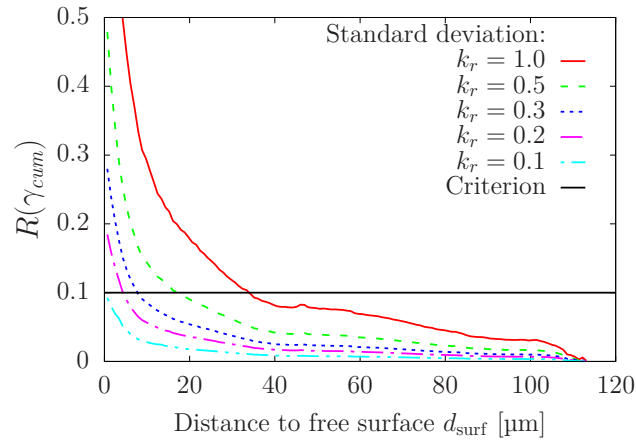
The main implications of this work are:

- introducing surface roughness inside a FECP analysis framework results in additional stress deviation and redistribution to the ones coming from the polycrystalline medium leading to important changes in plastic strain localization patterns;
- a perpendicular orientation of mechanical loading with respect to the orientation of surface streaks is the most critical case;
- this impact can be here considered as non negligible until a depth which length is linearly linked to roughness parameters;
- such considerations would also strictly change the results of any FECP or DD analysis such as Fatigue Indicator Parameters distribution [12].

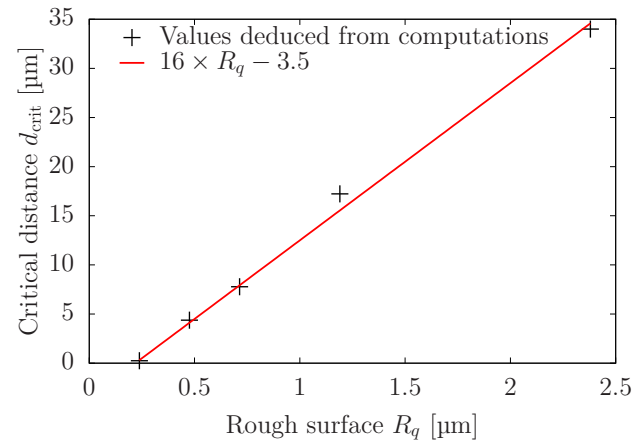
This study is part of a modeling framework that needs to be completed in the future, because it is still necessary to introduce parameters such as residual stresses or material hardening due to processing, which have not been taken into account here. However, the clear conclusion of the present numerical investigation is that polycrystalline aggregate computations must take into account surface roughness, specifically when they are focusing on surface fields.



(a)



(b)



(c)

Figure 10: Statistical analysis of the distribution of plastic strain comparison ratio $R(\gamma_{cum})$ for each surface state. (a) Integration point values and (b) standard deviation of $R(\gamma_{cum})$ versus distance to the free surface d_{surf} . (c) Critical distance d_{crit} versus surface Root Mean Square R_q .

Acknowledgments

The work has been supported by Agence Nationale pour la Recherche, in the framework of the project AFGRAP ANR-08-MAPR-0024.

References

- [1] Bayoumi M R and Abdellatif A K 1995 *Engng Fracture Mechanics* **51** 861–870
- [2] Blochwitz C, Brechbühl J and Tirschler W 1996 *Mater. Sci. Eng.* **A210** 42–47
- [3] Blochwitz C, Richter R, Tirschler W and Obrtlík K 1997 *Mater. Sci. Eng.* **A234–236** 563–566
- [4] Man J, Obrtlík K, Blochwitz C and Polák J 2002 *Acta Mat.* **50** 3767–3780
- [5] Man J, Obrtlík K and Polák J 2003 *Mater. Sci. Eng.* **A351** 123–132
- [6] King A, Ludwig W, Herbig M, Buffière J Y, Khan A, Stevens N and Marrow T 2011 *Acta Mat.* **59** 590–601
- [7] Herbig M, King A, Reischig P, Proudhon H, Lauridsen E, Marrow J, Buffière J Y and Ludwig W 2011 *Acta Mat.* **59** 590–601
- [8] Ma B T and Laird C 1989 *Acta Mat.* **37** 325–336
- [9] Essmann U, Gösele U and Mughrabi H 1981 *Phil. Mag.* **44** 405–426
- [10] Bennett V and McDowell D 2003 *Int. J. Fatigue* **25** 27–39
- [11] Dunne F, Wilkinson A and Allen R 2007 *Int. J. of Plasticity* **23** 273–295
- [12] Przybyla C and McDowell D 2010 *Int. J. of Plasticity* **26** 372–394
- [13] Guilhem Y, Basseville S, Curtit F, Stéphan J M and Cailletaud G 2010 *Int. J. Fatigue* **32** 1748–1763
- [14] Guilhem Y, Basseville S, Curtit F, Stéphan J M and Cailletaud G 2013 *Computational Materials Science* **70** 150–162
- [15] Basseville S, Cailletaud G, Ghidossi T, Guilhem Y, Lacoste E, Proudhon H, Signor L and Villechaise P 2017 *Mater. Sci. Eng. A* **696** 122–136
- [16] Déprés C, Robertson C and Fivel M 2006 *Phil. Mag.* **86** 79–97
- [17] Makhlof K, Sidhom N, Khelifi A, Sidhom H and Braham C 2013 *Materials and Design* **52** 1088–1098
- [18] Suhr R 1986 The effect of surface finish on high cycle fatigue of low alloy steel *The behaviour of short fatigue cracks* ed Miller K and de los Rios E (London) pp 69–86
- [19] Lee J and Nam S 1990 *Material Letters* **10** 223–230
- [20] Martin M, Weber S, Izawa S, Wagner S, Pundt A and Theisen W 2011 *International Journal of Hydrogen Energy* **36** 11195–11206
- [21] Suraratchai M, Limido J, Mabru C and Chieragatti R 2008 *Int. J. Fatigue* **30** 2119–2126
- [22] Proudhon H, Li J, Reischig P, Guéninchault N, Forest S and Ludwig W 2016 *Advanced Engineering Materials* **18** 903–912
- [23] Le Pécheur A, Curtit F, Clavel M, Stéphan J M, Rey C and Bompard P 2012 *Int. J. Fatigue* **45** 48–60
- [24] Yue Z 2005 *Engng Fracture Mechanics* **72** 749–757
- [25] Fang X, Yan W, Gao H, Yue Z and Wang F 2012 *Finite Element in Analysis and Design* **60** 64–71
- [26] Gao Y F and Bower A 2006 *Proc. Royal Soc. London, A* **462** 319–348
- [27] Pei L, Hyun S, Molinari J and Robbins M 2005 *J. Mech. Phys. Sol.* **53** 2385–2409
- [28] Dick T, Basseville S and Cailletaud G 2008 *Computational Materials Science* **43** 36–42
- [29] Li H, Öchsner A, Wei D, Ni G and Jiang Z 2015 *Applied Surface Science* **359** 236–244
- [30] Nicola L, Bower A, Kim K S, Needleman A and Van Der Giessen E 2008 *Phil. Mag.* **88** 3713–3729
- [31] Méric L and Cailletaud G 1991 *J. of Engng. Mat. Technol.* **113** 171–182
- [32] 2012 Z-set <http://www.zset-software.com/> version Z8.5
- [33] Besson J, Cailletaud G, Chaboche J L and Forest S 2009 *Nonlinear Mechanics of Materials* (Springer)

- [34] Franciosi P 1985 Acta Metall. **33** 1601–1612
- [35] Le Pécheur A 2008 Fatigue thermique d'un acier inoxydable austénitique : influence de l'état de surface par une approche multi-échelles Ph.D. thesis École Centrale de Paris
- [36] Jenkinson A F 1955 Quarterly Journal of the Royal Meteorological Society **81** 158–171
- [37] Hor A, Saintier N, Robert C, Palin-Luc T and Morel F 2014 Int. J. Fatigue **67** 151–158